



OPEN

## Guanidinylated SBA-15/Fe<sub>3</sub>O<sub>4</sub> mesoporous nanocomposite as an efficient catalyst for the synthesis of pyranopyrazole derivatives

Fereshte Hassanzadeh-Afruzi, Somayeh Asgharnasl, Sara Mehraeen, Zeinab Amiri-Khamakani & Ali Maleki✉

In this study, a novel mesoporous nanocomposite was fabricated in several steps. In this regard, SBA-15 was prepared by the hydrothermal method, next it was magnetized by *in-situ* preparation of Fe<sub>3</sub>O<sub>4</sub> MNPs. After that, the as-prepared SBA-15/Fe<sub>3</sub>O<sub>4</sub> functionalized with 3-minopropyltriethoxysilane (APTES) via post-synthesis approach. Then, the guanidinylated SBA-15/Fe<sub>3</sub>O<sub>4</sub> was obtained by nucleophilic addition of APTES@SBA-15/Fe<sub>3</sub>O<sub>4</sub> to cyanimide. The prepared nanocomposite exhibited excellent catalytic activity in the synthesis of dihydropyrano[2,3-*c*]pyrazole derivatives which can be related to its physicochemical features such as strong basic sites (presented in guanidine group), Lewis acid site (presented in Fe<sub>3</sub>O<sub>4</sub>), high porous structure, and high surface area. The characterization of the prepared mesoporous nanocomposite was well accomplished by different techniques such as FT-IR, EDX, FESEM, TEM, VSM, TGA, XRD and BET. Furthermore, the magnetic catalyst was reused at least six consequent runs without considerable reduction in its catalytic activity.

Porous materials with remarkable characteristics such as high surface area, well-defined porous structure, uniform pore size, and processability have attracted great interest from researchers in scientific fields<sup>1,2</sup>. Based on the IUPAC definition, the porous materials are classified in three main groups depending on their pore size (or pore width): microporous (pores width < 2 nm), mesoporous (2 < pores width < 50 nm), and macroporous (pores width > 50 nm) materials<sup>2,3</sup>. In 1998, Stucky and et al. synthesized a novel kind of hexagonal array of pores named SBA (Santa Barbara Amorphous). After that, different types of SBA materials such as SBA-1, SBA-16 and SBA-15 have synthesized. The SBA-15 is a highly ordered mesoporous materials with striking properties for instance high surface area, straight cylindrical pores, thick framework walls, adjustable pore size (4–30), large pore diameter (which provide a facilitated diffusion of reactant molecules), and excellent ability to be modified/functionalized. It has been extensively utilized in various application such as catalysis<sup>4</sup>, removal of pollutants form wastewater<sup>5</sup>, hyperthermia<sup>6</sup>, drug delivery<sup>7,8</sup>, and chromatographic techniques<sup>9</sup>. To obtain high performance SBA-15-based catalysts, the surface functionalization or modification needs to be performed. There are two main approach to modify/functionalize the silica-based mesoporous materials including one-pot synthesis or co-condensation and grafting technique or post-synthesis. In the first approach, the active phase is added to the reaction mixture which subsequently co-assembles into the inorganic framework for the construction of the mesoporous material in single step, but in the second approach siliceous support is prepared followed by the modification with active moieties or their precursors<sup>2,10,11</sup>. Incorporating Fe<sub>3</sub>O<sub>4</sub> MNPs as a superparamagnetic material into the silica-based mesoporous materials is a practical way to achieve retrievable and reusable nanocomposite with enhanced surface area<sup>12</sup>. The chemical modification of SBA-15 gives high efficiency porous catalyst by more active sites to interact with reactants. In recent years, a great attention has been dedicated to prepare amine functionalized SBA-15 to enhance its potential catalytic application. For instance, several types of amines functionalized SBA-15 were fabricated via grafting technique by using three different aminosilane reagents then, it was applied as heterogeneous catalysts for Michael addition<sup>13</sup>. One of the most widely used materials to modify the SBA-15 through both co-condensation or and post-synthesis is the 3-aminopropyltriethoxysilane (APTES)<sup>14,15</sup>.

Catalysts and Organic Synthesis Research Laboratory, Department of Chemistry, Iran University of Science and Technology, 16846-13114 Tehran, Iran. ✉email: maleki@iust.ac.ir

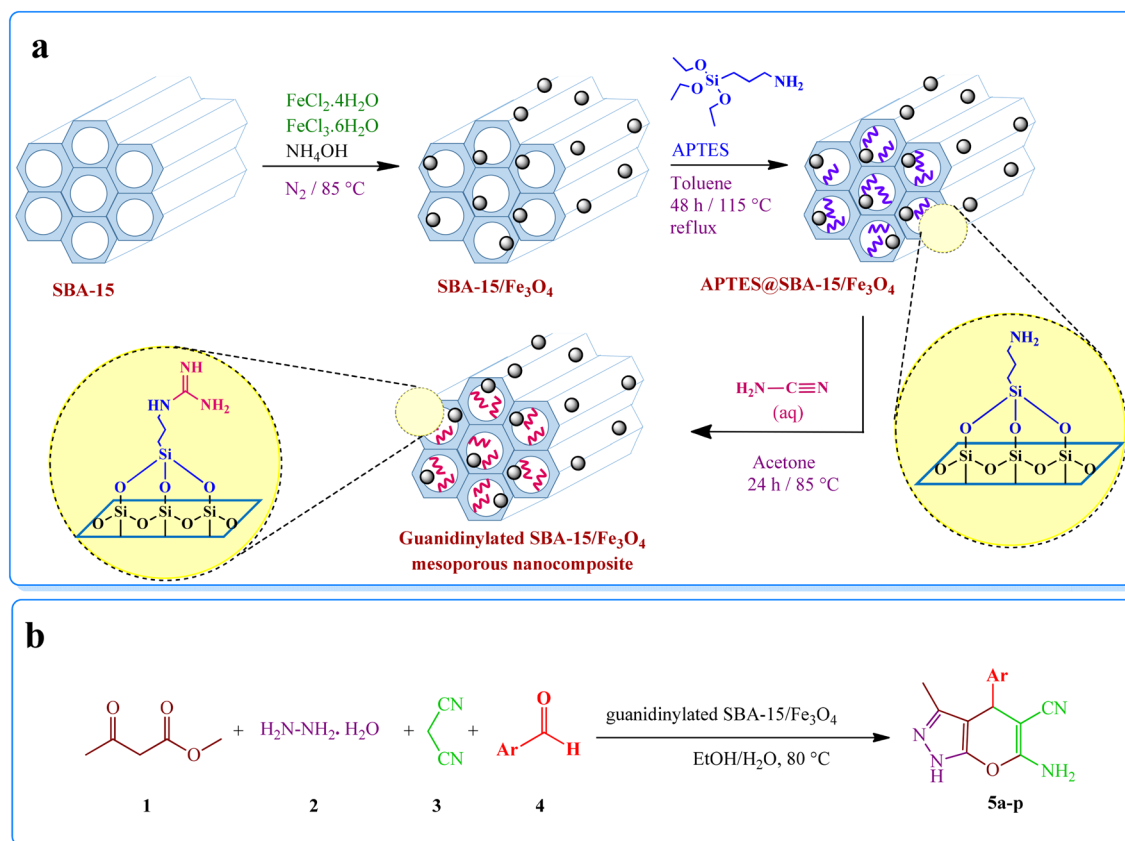


**Figure 1.** Preparation route of (a) the guanidinylated SBA-15/Fe<sub>3</sub>O<sub>4</sub> and (b) its catalyst application in the synthesis of dihydropyrano[2,3-c]pyrazole derivatives.

Guanidine, the nitrogenous analogue of carbonic acids, is a fascinating group of basic organic compounds. They are exceedingly strong Brønsted and Lewis bases, their basic strength more than amines, pyridines, diamines and amidines. This strong basicity is ascribed to great delocalization of positive charge on the guanidinium cation above the three nitrogen atoms. After protonation of guanidine group, the highly stable guanidinium ion act as a bidentate hydrogen bond donor which able to activate different hydrogen bond acceptors species such as carbonyl groups<sup>16,17</sup>. Therefore, guanidine and their derivatives can be considered as appropriate candidates in base-catalyzed organic reactions. The guanidinylation reaction has been used to convert primary amine groups in different materials for example chitosan<sup>18,19</sup> and Poly(2-guanidinoethylmethacrylate)<sup>20</sup> into guanidine groups. Multicomponent reactions (MCRs) are one of the most significant methods for the synthesis of heterocyclic compounds because of their outstanding properties such as high atomic economy, short reaction time, straightforward reaction model, high selectivity, and great compliance with principals of green chemistry<sup>21–23</sup>. Among the product of MCRs, the pyranopyrazole derivatives have received much interest of researchers due to their extensive application in pharmacology and medicine<sup>24–27</sup>. In continuation of research on heterogeneous nanocatalysts<sup>28–30</sup>, in this study a novel SBA-15 based nanocomposite prepared in four steps as illustrated in Fig. 1a, then it was used as a heterogeneous catalyst in the synthesis of dihydropyrano[2,3-c]pyrazole derivatives via four component condensation reaction (Fig. 1b).

## Experimental

**General.** All the required chemical reagents and solvents were purchased from the chemical international companies including Merck and Sigma Aldrich. Several analyses were carried out to demonstrate the construction of the catalyst. Fourier-transform infrared (FT-IR) spectra were carried out by applying a Shimadzu IR-470 spectrometer by using KBr pellet. Elemental analysis of the prepared samples was performed by energy dispersive x-ray analysis (EDX) recorded on Numerix JEOL-JDX 8030 (30 kV, 20 mA). X-ray diffraction (XRD) pattern of fabricated samples were obtained by X-ray diffractometer (Bruker D8 Advance). The morphology and surface of samples were studied by a field emission scanning electron microscope (FESEM) and transmission electron microscopies (TEM) using VEGA2 TESCAN instrument and Zeiss-EM10C-100 kV, respectively. The magnetic behavior of samples was measured using VSM analysis (Meghnatis, daneshpajoooh Kashan), and thermal stability of samples was studied by thermogravimetric analysis (TGA) using a Bahr-STA 504 instrument. Melting points of synthesized products were measured with an Electrothermal 9100 apparatus. The specific surface area of prepared samples was determined using the Brunauer–Emmett–Teller (BET, Micrometics ASAP2020). <sup>1</sup>H NMR and <sup>13</sup>C NMR nuclear magnetic resonance spectra were recorded on a Bruker DRX-500

spectrometer at 500 and 125 MHz, respectively. Analytical thin-layer chromatography (TLC) was done by Merck silica gel GF254 plates.

**Catalyst preparation.** *Preparation of SBA-15.* According to the previously reported studies<sup>31</sup>, the SBA-15 was synthesized by the hydrothermal method. First, 3.5 g of P123 surfactant as a structure-directing agent was dissolved in 120 mL of 1.6 M hydrochloric acid. Next, the obtained solution stirred at 40 °C for 24 h to get a homogenous mixture. After that, 8 mL (7.5 g) of TEOS (tetraethyl orthosilicate) as an alkoxy silanes reagent was added into the above clear solution and stirring was continued at 40 °C for 24 h to complete hydrolysis of silica source. Then, the resulting mixture was transferred into the teflon-lined autoclave, and heated at 150 °C for 24 h. After the autoclave temperature gradually decreased, the resulting mixture was filtered, washed several consecutive times with distilled water (15 × 25 mL), and then dried at room temperature. The final white powder was calcined at 550 °C for 4 h with a heating rate of 2.3 °C min<sup>-1</sup> for removal of surfactant and forming the ordered mesoporous channels.

*Preparation of SBA-15/Fe<sub>3</sub>O<sub>4</sub>.* To magnetize SBA-15, the *in-situ* co-precipitation method was performed. For this, 2 mmol (0.4 g) of FeCl<sub>2</sub>·4H<sub>2</sub>O and 4 mmol (0.54 g) of FeCl<sub>3</sub>·6H<sub>2</sub>O were dissolved in 50 ml distilled water. The obtained homogeneous solution was transferred to a 2-necked round-bottom flask containing 0.5 g dispersed SBA-15 in 50 mL distilled water. The final mixture was kept stirring at room temperature for about 45 min under N<sub>2</sub> atmosphere. Then, the temperature was gradually raised to 85 °C. After that, 10 mL of ammonium hydroxide (25%) was added dropwise to the stirring solution. The reaction was kept under this condition for 2 h to form Fe<sub>3</sub>O<sub>4</sub> MNPs on the mesoporous SBA-15 support. The synthesized magnetic product was collected by a magnet, washed with distilled water and acetone, and then dried in an oven at 90 °C for 5 h.

*Preparation APTES functionalized SBA-15/Fe<sub>3</sub>O<sub>4</sub> (APTES@SBA-15/Fe<sub>3</sub>O<sub>4</sub>).* The functionalization of SBA-15/Fe<sub>3</sub>O<sub>4</sub> by APTES was carried out by the post-synthesis approach. At first, 0.5 g of SBA-15/Fe<sub>3</sub>O<sub>4</sub> and 2 mL of APTES were dispersed in 35 mL of toluene by stirring. Then, the obtained mixture was refluxed at 115 °C for 48 h. It is expected that free silanol groups (Si-OH) of SBA-15/Fe<sub>3</sub>O<sub>4</sub> covalently react with the silica group on the APTES to form Si-O-Si bond (siloxane bond) through condensation reaction. The dark brown precipitate was isolated by a magnet, washed several times with ethanol and acetone and then dried in oven at 100 °C.

*Guanidinylation of APTES@SBA-15/Fe<sub>3</sub>O<sub>4</sub>.* The guanidinylated SBA-15/Fe<sub>3</sub>O<sub>4</sub> was obtained by nucleophilic addition between APTES@SBA-15/Fe<sub>3</sub>O<sub>4</sub> and cyanamide. Initially, 0.5 g of cyanamide was dissolved in 5 ml distilled water and added to 0.1 g APTES@SBA-15/Fe<sub>3</sub>O<sub>4</sub> which dispersed in 35 mL acetone; next the mixture was kept stirring for 24 h at 85 °C. Then, the final product collected by a magnet, washed several times with distilled water and acetone, and dried in oven at 100 °C.

**General procedure for the synthesis of pyranopyrazoles derivatives.** The catalytic performance of fabricated mesoporous catalyst was evaluated in one-pot synthesis of the pyranopyrazoles. For this, four components including ethyl acetoacetate (1 mmol), hydrazine hydrate (1.2 mmol), aromatic aldehyde (1.0 mmol) and malononitrile (1.0 mmol) were mixed and reacted by adding 0.01 g of the guanidinylated SBA-15/Fe<sub>3</sub>O<sub>4</sub> mesoporous catalyst in the presence of 1 ml EtOH/ H<sub>2</sub>O (1:1) at 80 °C. The reaction completion process was investigated by thin layer chromatography (TLC). After completion of the reaction, hot ethanol was added to dissolve the product, then undissolved magnetic mesoporous catalyst was separated from the reaction mixture by a magnet and filtration. The crude products were recrystallized from EtOH to obtain pure dihydropyrano[2,3-c] pyrazole derivatives.

**Spectral data of selected products.** 6-Amino-4-(4-chlorophenyl)-3-methyl-2,4-dihydropyrano[2,3-c]pyrazole-5-carbonitrile (**5b**): <sup>1</sup>H-NMR (500 MHz, DMSO-d<sub>6</sub>): δ<sub>H</sub> (ppm) = 1.79 (s, 3H, methyl), 4.63 (s, 1H, methine), 6.91 (s, 2H, NH<sub>2</sub>), 7.19–7.20 (d, J = 8 Hz, 2H, H-aromatic), 7.37–7.38 (d, J = 8 Hz, 2H, H-aromatic), 12.12 (s, 1H, NH); <sup>13</sup>C NMR (125 MHz, DMSO-d<sub>6</sub>): δ<sub>C</sub> (ppm) = 10.18, 36.04, 57.30, 97.66, 121.06, 128.91, 129.82, 131.69, 136.12, 143.95, 155.19, 161.38.

6-Amino-3-methyl-4-(3-nitrophenyl)-1,4-dihydropyrano [2, 3-c] pyrazole-5-carbonitrile (**5e**): <sup>1</sup>H-NMR (500 MHz, DMSO-d<sub>6</sub>): δ<sub>H</sub> (ppm) = 1.81 (s, 3H, methyl), 4.88 (s, 1H, methine), 7.05 (s, 2H, NH<sub>2</sub>), 7.65 (m, 2H, H-aromatic), 8.02 (s, 1H, H-aromatic), 8.11 (dd, J = 7.7 Hz 1H, H-aromatic), 12.20 (s, 1H, NH); <sup>13</sup>C NMR (125 MHz, DMSO-d<sub>6</sub>): δ<sub>C</sub> (ppm) = 9.74, 35.66, 56.17, 96.65, 120.49, 121.83, 121.93, 130.22, 134.36, 135.89, 146.8, 147.88, 154.69, 161.13.

6-Amino-4-(4-hydroxyphenyl)-3-methyl-2,4-dihydropyrano[2,3-c]pyrazole-5-carbonitrile (**5k**): <sup>1</sup>H-NMR (500 MHz, DMSO-d<sub>6</sub>): δ<sub>H</sub> (ppm) = 1.78 (s, 3H, methyl), 4.47 (s, 1H, methine), 6.68–6.69 (d, J = 8 Hz, 2H, H-aromatic), 6.76 (s, 2H, NH<sub>2</sub>), 6.94–6.96 (d, J = 8 Hz, 2H, H-aromatic), 9.25 (s, 1H, OH) 12.03 (s, 1H, NH); <sup>13</sup>C NMR (125 MHz, DMSO-d<sub>6</sub>): δ<sub>C</sub> (ppm) = 10.2, 35.9, 58.3, 98.5, 115.6, 121.3, 128.9, 135.2, 135.9, 155.2, 156.5, 161.1.

## Results and discussion

**Characterizations.** In the present work, a new magnetic mesoporous nanocomposite based on SBA-15 was prepared. In this regard, four main steps were carried out to obtain this catalyst include preparation of SBA-15, *in-situ* fabrication of Fe<sub>3</sub>O<sub>4</sub> on SBA-15 support, functionalization of the SBA-15/Fe<sub>3</sub>O<sub>4</sub> composite with APTES, and eventually the guanidinylation reaction of APTES@SBA-15/Fe<sub>3</sub>O<sub>4</sub>. To characterize the magnetic

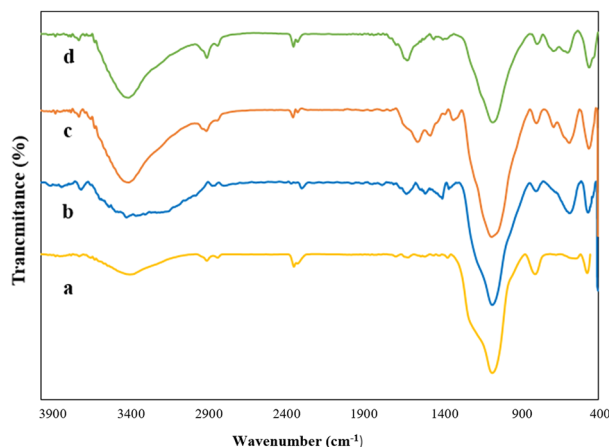


**Figure 2.** FT-IR of (a) SBA-15, (b) SBA-15/Fe<sub>3</sub>O<sub>4</sub>, (c) APTES@SBA-15/Fe<sub>3</sub>O<sub>4</sub> and (d) guanidinylated SBA-15/Fe<sub>3</sub>O<sub>4</sub>.

mesoporous catalyst, several spectral and analytical techniques were employed which will be explained and discussed.

**FT-IR spectroscopy.** FT-IR analysis was used to detect different functional groups in the samples fabricated in each step. As is observed in Fig. 2, IR spectrum of SBA-15 (a) has characteristic absorption bands at 470 (bending vibration of Si–O–Si), 800 (stretching vibration of Si–O–Si), 958 (vibration of Si–O–H), 1080 (symmetric stretching vibration of Si–O–Si), and 3420 cm<sup>−1</sup> (stretching vibration of OH groups)<sup>32–34</sup>. IR spectrum of SBA-15/Fe<sub>3</sub>O<sub>4</sub> in addition to similar absorptions which observed in spectrum a showed a new absorption bands at 577 cm<sup>−1</sup> which assigned to Fe–O stretching vibration. After the functionalization of the SBA-15/Fe<sub>3</sub>O<sub>4</sub> with APTES, two new absorption bands have emerged in 1562 and 2925 cm<sup>−1</sup> which are related to the bending vibration of NH<sub>2</sub> and the stretching vibrations of the C–H bond in the propyl chain of APTES, respectively (spectrum b) Furthermore, in this spectrum the intensity of absorption of the Si–OH bands at 958 cm<sup>−1</sup> was decreased, signifying that the surface silanols are substituted by aminosilane groups after functionalization<sup>35,36</sup>. Moreover, guanidinylated APTES @SBA-15/Fe<sub>3</sub>O<sub>4</sub> was evaluated by comparing IR spectra of guanidinylated SBA-15/Fe<sub>3</sub>O<sub>4</sub> (c) and APTES@SBA-15/Fe<sub>3</sub>O<sub>4</sub> (b). Nucleophilic addition of APTES@SBA-15/Fe<sub>3</sub>O<sub>4</sub> to cyanamide resulted in disappearing the bending vibration of NH<sub>2</sub> at 1560 cm<sup>−1</sup> and intensification the absorption band at 1627 cm<sup>−1</sup> which can be attributed to the stretching vibrations of the imine bond of guanidine group formed during this final step modification<sup>37</sup>.

**EDX analysis.** Detection of the organic and inorganic elements in the prepared samples was carried out by the EDX analysis as a qualitative method. As is shown in Fig. 3, O and Si are the elemental compositions of SBA-15 (spectrum a), and distinctive peaks of Fe, O, and Si are related to the elemental composition of the SBA-15/Fe<sub>3</sub>O<sub>4</sub> (spectrum b), observing two Fe peaks are related to the existence of Fe<sub>3</sub>O<sub>4</sub> MNPs in the structure of the SBA-15/Fe<sub>3</sub>O<sub>4</sub>. By modification of the SBA-15/Fe<sub>3</sub>O<sub>4</sub> with APTES, the peaks of C and N elements were added to the previous peaks in the spectrum c. The guanidinylated SBA-15/Fe<sub>3</sub>O<sub>4</sub> can cause the emerging of Fe, O, Si, C and N peaks in the EDX spectrum d. Moreover, the distribution of elements in this mesoporous nanocomposite is shown in the EDX mapping images (e).

**Transmission and Scanning Electron Microscopies (TEM, SEM).** Field emission scanning electron microscopy was employed to observe particle size distribution, surface morphology and particle aggregation mode in prepared samples. As is observed in Fig. 4, the FESEM images of guanidinylated SBA-15/Fe<sub>3</sub>O<sub>4</sub> and SBA-15 are presented in three scales: 1 μm, 500 and 200 nm. The SBA-15 images presented a porous structure, but in the nanocomposite images in addition to the porous structure, the distribution of spherical Fe<sub>3</sub>O<sub>4</sub> MNPs on the SBA-15 as a mesoporous support was also can be observed. Therefore, fabrication Fe<sub>3</sub>O<sub>4</sub> MNPs onto SBA-15 mesoporous matrix and subsequent modification resulted in change the its morphology. The average particle size for 35 spherical particles in the nanocomposite was determined to be about 26 nm using Digimizer software. TEM analysis was performed to more accurately study the morphology and particle size of the mesostructured guanidinylated SBA-15/Fe<sub>3</sub>O<sub>4</sub> catalyst. As can be seen in Fig. 5, TEM image of prepared nanocomposite (left image of Fig. 4c) exhibited an ordered pore channels framework having dimension about 6–7 nm. In another image (right image of Fig. 4c), both a regular mesoporous arrangement with two-dimensional hexagonal honeycomb structure and the Fe<sub>3</sub>O<sub>4</sub> MNPs onto SBA-15 support was observed, but formation of the magnetite NPs onto the certain amount of SBA-15 channels and subsequent functionalization lead to hide some part of ordered pore arrangement.

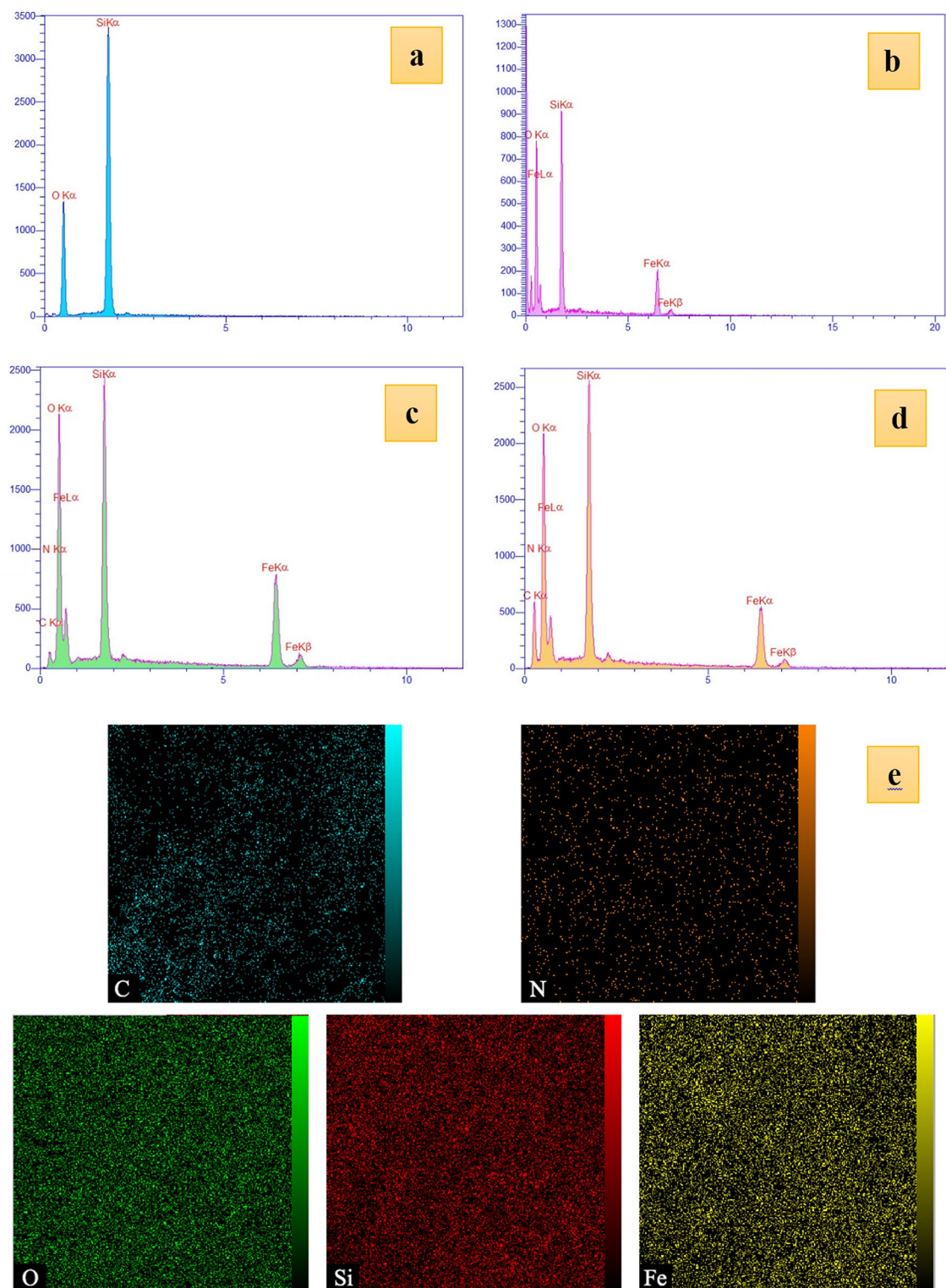


**Figure 3.** EDX analyses of (a) SBA-15, (b) SBA-15/Fe<sub>3</sub>O<sub>4</sub>, (c) APTES@ SBA-15/Fe<sub>3</sub>O<sub>4</sub>, (d) guanidinylated SBA-15/Fe<sub>3</sub>O<sub>4</sub>, (e) and mapping images of the guanidinylated SBA-15/Fe<sub>3</sub>O<sub>4</sub>.

**VSM analysis.** To evaluate the magnetic properties of the prepared samples, vibrating sample magnetometer (VSM) was employed at room temperature and in the field range of  $-10 < kOe < +10$ . As indicated in Fig. 5, the measured magnetic saturation ( $M_s$ ) for bare Fe<sub>3</sub>O<sub>4</sub>, SBA-15/Fe<sub>3</sub>O<sub>4</sub> and guanidinylated SBA-15/Fe<sub>3</sub>O<sub>4</sub> were about 52.1, 30.1, and 12.16 emu/g, respectively. The reduction in  $M_s$  of the SBA-15/Fe<sub>3</sub>O<sub>4</sub> compared to bare Fe<sub>3</sub>O<sub>4</sub> is due to the presence of SBA-15 as a non-magnetic component in the SBA-15/Fe<sub>3</sub>O<sub>4</sub> structure. Then, by further chemical modification on SBA-15/Fe<sub>3</sub>O<sub>4</sub> and the addition of more non-magnetic segments, the amount of  $M_s$

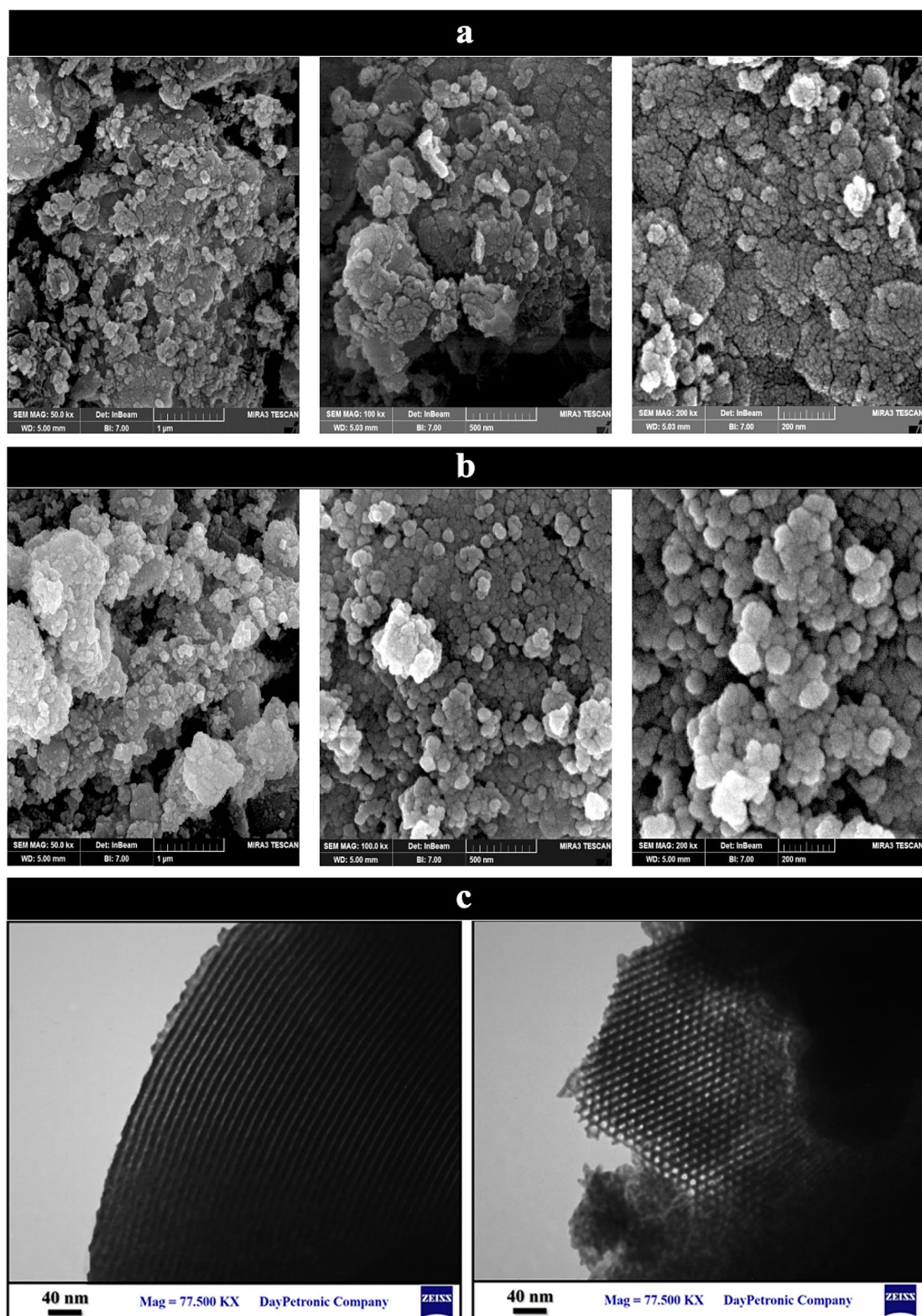


**Figure 4.** FESEM images of (a) SBA-15, (b) the guanidylated SBA-15/Fe<sub>3</sub>O<sub>4</sub>, and (c) TEM image of the guanidylated SBA-15/Fe<sub>3</sub>O<sub>4</sub>.

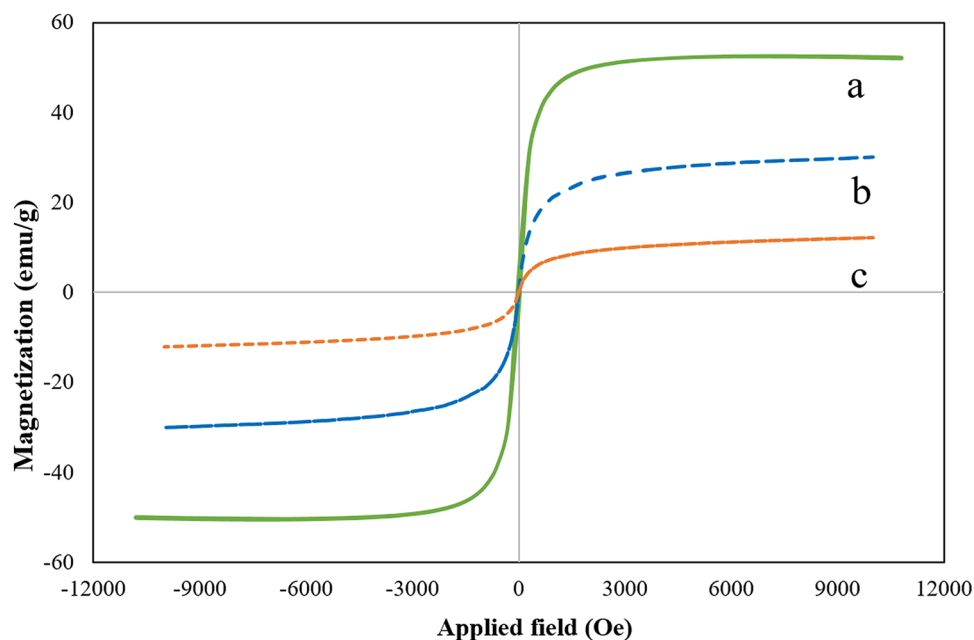


**Figure 5.** The magnetization curves of (a)  $\text{Fe}_3\text{O}_4$  MNPs, (b)  $\text{SBA-15/Fe}_3\text{O}_4$ , (c) and the guanidinylated  $\text{SBA-15/Fe}_3\text{O}_4$ .

in guanidinylated  $\text{SBA-15/Fe}_3\text{O}_4$  was decreased to about 12.16 (emu/g), which seems reasonable. However, the nanocomposite is sufficiently magnetized to be effortlessly separated from the reaction mixture by a magnet and reused for several consecutive times. Besides, considering that the values of coercivity ( $H_c$ ) and remanence ( $M_r$ ) in the VSM curves of the prepared samples are zero, their superparamagnetic behavior is confirmed.

**TGA analysis.** Thermal analysis of the  $\text{SBA-15/Fe}_3\text{O}_4$  and guanidinylated  $\text{SBA-15/Fe}_3\text{O}_4$  was performed by TGA analysis in the temperature range 50–800 °C with a heating rate of 10 °C  $\text{min}^{-1}$  under air atmosphere. For a more detailed study, the thermal behavior of  $\text{SBA-15}$  and  $\text{Fe}_3\text{O}_4$  which reported in literature was also studied. According to the reported information,  $\text{SBA-15}$  has high thermal stability; it has maintained above 90–95% of its weight up to 700 °C and a continuous slight weight loss was attributed to dehydrogenation or dehydroxylation of its surface<sup>38,39</sup>. Moreover, the thermal behavior of  $\text{Fe}_3\text{O}_4$  displayed that with increasing the temperature to 800 °C, a small weight loss of about 5–6% was occurred, which was ascribed to the evaporation of water molecules absorbed in it<sup>40</sup>. As can be observed in Fig. 6, the thermogram of the  $\text{SBA-15/Fe}_3\text{O}_4$  (a) exhibited a gradual gentle weight loss between 50 and 800 °C which may be related to the evaporation of adsorbed water molecules in the cavities of this sample, and dehydrogenation or dehydroxylation of its surface. Therefore, high thermal stability of this composite was demonstrated with just 9% weight loss until 800 °C. In the thermogram of guanidinylated  $\text{SBA-15/Fe}_3\text{O}_4$  nanocomposite (b), the first observed weight loss (~2%) in the temperature range of 50–160 °C is attributed to the evaporation adsorbed water molecules in the cavities and surface of the mesoporous nanocomposite. Next, with increasing temperature to 550 °C weight loss of about 10% occurs, which can be due to the separation and thermal decomposition of organic parts (alkyl chain and guanidine group) that covalently bounded to the  $\text{SBA-15/Fe}_3\text{O}_4$ , and the continuation of weight loss with increasing temperature up to 800 °C can be ascribed to the condensation of silanol groups of guanidinylated  $\text{SBA-15/Fe}_3\text{O}_4$ <sup>41</sup>. The residual weight of these mesoporous nanocomposites up to 800 °C is about 85%, which is only 6% more weight loss than the  $\text{SBA-15/Fe}_3\text{O}_4$  compound. Therefore, it can be referred that the two steps chemical modification of  $\text{SBA-15/Fe}_3\text{O}_4$  did not have a significant effect on its thermal resistance. Furthermore, considering the difference in residual weight of the two samples, it can be calculated that just about 6% of the total weight of the guanidinylated  $\text{SBA-15/Fe}_3\text{O}_4$  nanocomposite composed of the organic part. The differential thermogravimetric analysis (DTGA) of guanidinylated  $\text{SBA-15/Fe}_3\text{O}_4$  (spectrum c) showed main endothermic peaks at 123 and two weak peaks at 411 and 510, the first one is attributed to the loss of adsorbed water molecules in mesoporous nanocomposite and the others related to decomposition of the organic part which constitute a very small weight percent of nanocomposite and the condensation of silanol groups of  $\text{SBA-15}$ . It can be seen from these results that the prepared mesoporous nanocomposite has structural stability at high temperatures and can be used for catalytic reactions at high temperature.

**XRD analysis.** The XRD analysis was used to investigate the crystalline nature of prepared samples. As is depicted in Fig. 7, the XRD pattern of  $\text{SBA-15}$  (b) showed a broad characteristic peak at  $2\theta$ : 20–30<sup>34,42</sup>. The diffractogram of guanidinylated  $\text{SBA-15/Fe}_3\text{O}_4$  (c) exhibited the relatively broad peak at  $2\theta$ : 20–30° with attributed to the presence of  $\text{SBA-15}$ , which was lower intensity compared to unmodified  $\text{SBA-15}$ , this reduction can

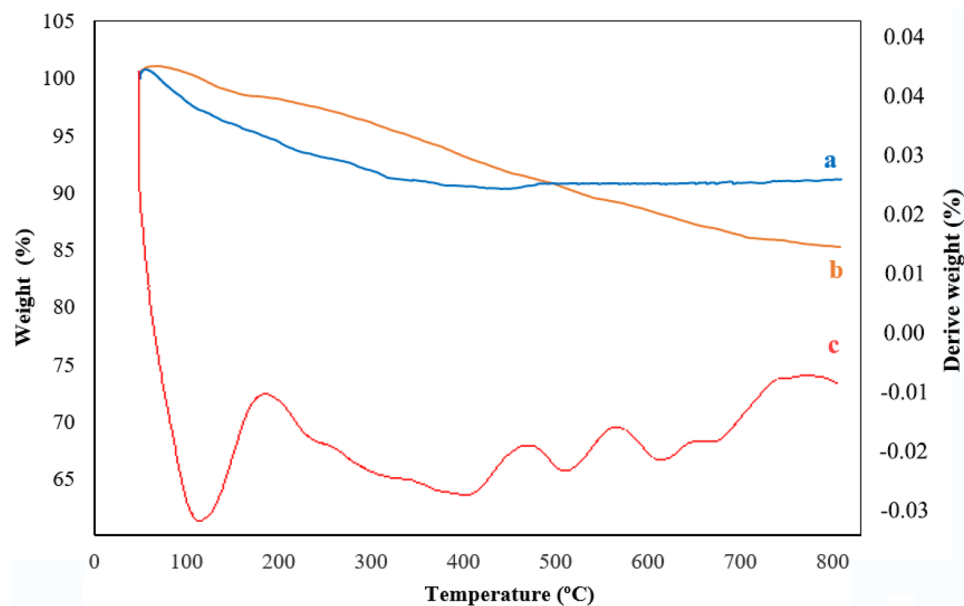


**Figure 6.** TGA curves of (a) SBA-15/Fe<sub>3</sub>O<sub>4</sub>, (b) the guanidynylated SBA-15/Fe<sub>3</sub>O<sub>4</sub>, and (c) DTGA of the guanidynylated SBA-15/Fe<sub>3</sub>O<sub>4</sub>.

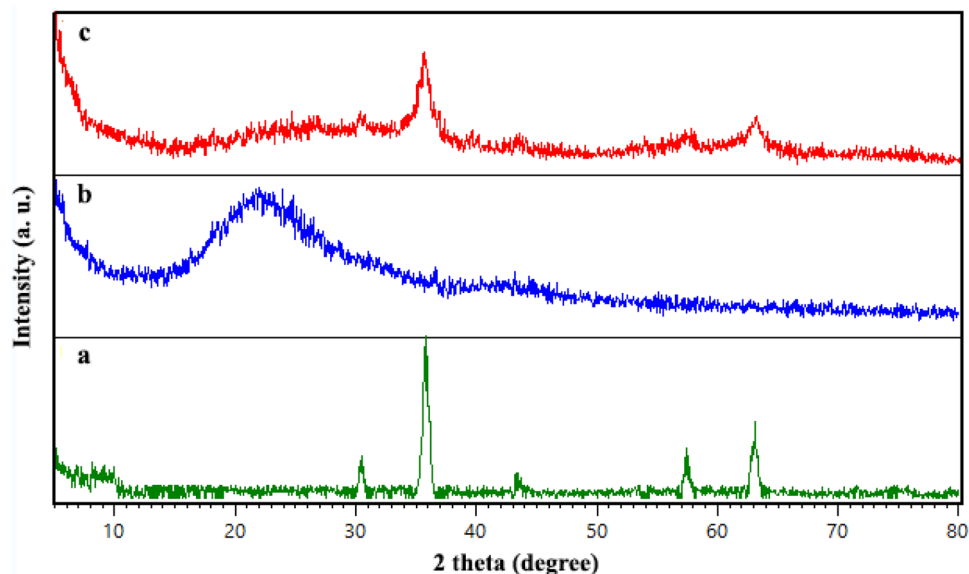


**Figure 7.** XRD pattern of (a) Fe<sub>3</sub>O<sub>4</sub>, (b) SBA-15 and (c), the guanidynylated SBA-15/Fe<sub>3</sub>O<sub>4</sub>.

be ascribed to three steps of modification of SBA-15. Moreover, there are several peaks at  $2\theta$ : 30.38°, 35.74°, 43.40°, 58°, 63.22° correspond exactly to the index peaks in the XRD pattern of Fe<sub>3</sub>O<sub>4</sub> confirming the presence of these nanoparticles in the guanidynylated SBA-15/Fe<sub>3</sub>O<sub>4</sub> structure. It can be concluded that formation of Fe<sub>3</sub>O<sub>4</sub> MNPs on SBA-15 matrix even with modifications has enhanced its crystallinity. The average crystallite size of neat Fe<sub>3</sub>O<sub>4</sub> and the guanidynylated SBA-15/Fe<sub>3</sub>O<sub>4</sub> nanocomposite by the Scherrer equation was calculated to be about 19 and 37 nm, respectively. The increase in average crystallite size of mesoporous nanocomposite in compared with neat Fe<sub>3</sub>O<sub>4</sub> can be mainly due to the SBA-15 matrix. Furthermore, the X-ray diffraction patterns of all prepared samples at low angles in the  $2\theta$ : 0–5° are shown in Fig. 8. The XRD pattern of SBA-15 shows one high intensity peak at  $2\theta$ : 0.91 and two small peaks at  $2\theta$ : 1.58 and 1.82 corresponding to (1 0 0), (1 1 0) and (2 0 0) planes, respectively. They are typical hexagonally structured SBA-15 with highly ordered mesoporous channels. As observed, diffractograms of SBA-15/Fe<sub>3</sub>O<sub>4</sub>, APTES@SBA-15/Fe<sub>3</sub>O<sub>4</sub> and guanidynylated SBA-15/Fe<sub>3</sub>O<sub>4</sub> samples showed the first peak corresponding to the (100) reflection which intensity decreases with each step modification, but two minor peaks corresponding to (1 1 0) and (2 0 0) planes are became weaker or almost

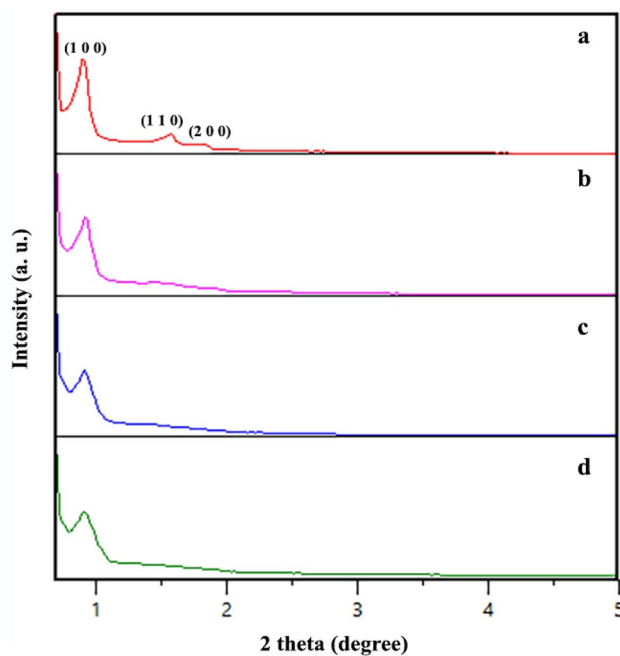


**Figure 8.** Low-angle XRD patterns of (a) SBA-15, (b) SBA-15/Fe<sub>3</sub>O<sub>4</sub>, (c) APTES@SBA-15/Fe<sub>3</sub>O<sub>4</sub>, and (d) the guanidinylated SBA-15/Fe<sub>3</sub>O<sub>4</sub>.

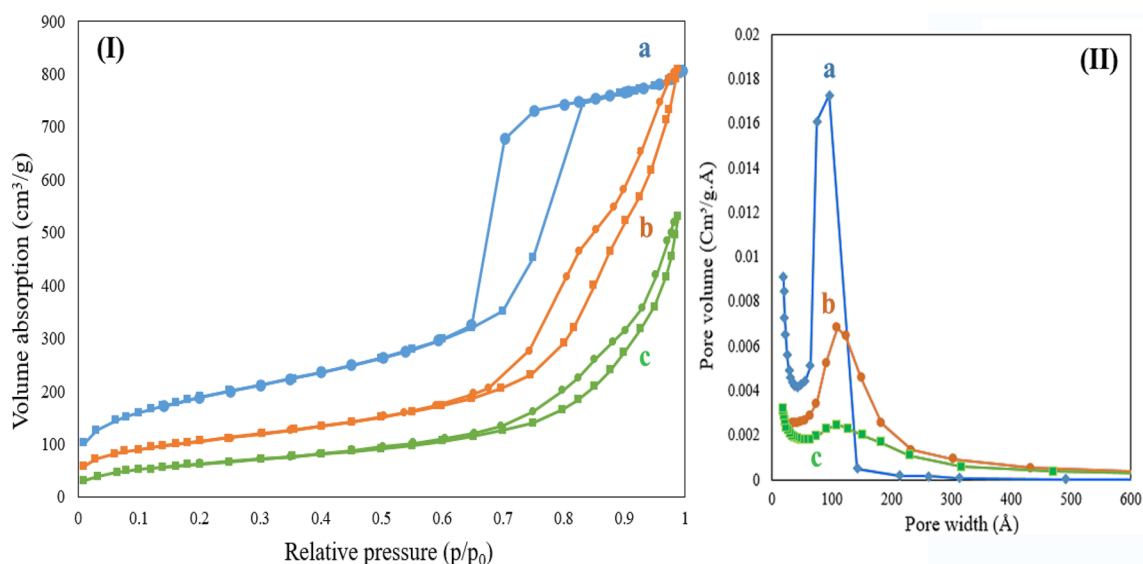


**Figure 9.** (I) N<sub>2</sub> adsorption–desorption isotherms and (II) the pore size distribution curve of (a) SBA-15, (b) SBA-15/Fe<sub>3</sub>O<sub>4</sub> and (c) the guanidinylated SBA-15/Fe<sub>3</sub>O<sub>4</sub>.

disappeared in these samples which can be attributed to partial disruption of the structure by incorporation of Fe<sub>3</sub>O<sub>4</sub> MNPs and the lowering of the local order.

**The N<sub>2</sub> adsorption–desorption isotherm.** The N<sub>2</sub> adsorption–desorption isotherm of the SBA-15, SBA-15/Fe<sub>3</sub>O<sub>4</sub> and guanidinylated SBA-15/Fe<sub>3</sub>O<sub>4</sub> are presented in Fig. 9. All samples exhibited a typical type-IV curves which are characteristic of mesoporous materials. However, the magnetic nanocomposites exhibited narrower hysteresis cycles than the SBA-15 and their adsorption and desorption branches are closer which can be related to an increase in their pore diameters, as can be seen in Fig. 9(I). The surface area, the pore volume and pore size (width) were calculated by the BET (Brunauer–Emmett–Teller) and BJH (Barrett–Joyner–Halenda) methods and results are summarized in Table 1. The BET surface area of the bare SBA-15 is about 687 m<sup>2</sup>/g which is more than the BET surface area of the SBA-15/Fe<sub>3</sub>O<sub>4</sub> and guanidinylated SBA-15/Fe<sub>3</sub>O<sub>4</sub>. This observation can be mainly related to blocking of a certain amount of SBA-15 pores by the embedding of Fe<sub>3</sub>O<sub>4</sub> MNPs on the

Sample	Surface area <sup>a</sup> (m <sup>2</sup> /g)	Pore volume <sup>b</sup> (cm <sup>3</sup> /g)	Pore size <sup>b</sup> (nm)
SBA-15	686.90	1.28	7.35
SBA-15/Fe <sub>3</sub> O <sub>4</sub>	383.91	1.26	12.64
guanidinylated SBA-15/Fe <sub>3</sub> O <sub>4</sub>	232.11	0.83	13.30

**Table 1.** Surface area, pore volume and pore diameter of SBA-15/Fe<sub>3</sub>O<sub>4</sub> and guanidinylated SBA-15/Fe<sub>3</sub>O<sub>4</sub> nanocomposite. <sup>a</sup>The surface area obtained by BET analysis. <sup>b</sup>Pore volume and pore diameter obtained by BJH analysis.

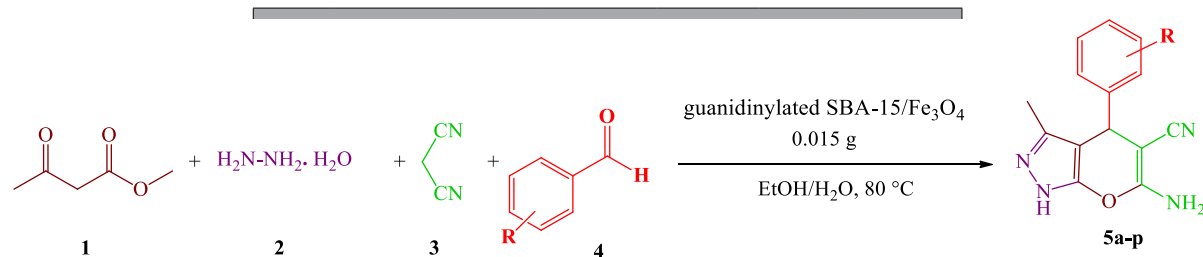
Entry	Catalyst	Catalyst loading (g)	Solvent	Temp (°C)	Yield <sup>b</sup> (%)
1	–		–	r.t	Trace
2	–		–	80	Trace
3	guanidinylated SBA-15/Fe <sub>3</sub> O <sub>4</sub>	0.02	–	r.t	47
4	guanidinylated SBA-15/Fe <sub>3</sub> O <sub>4</sub>	0.02	EtOH	r.t	70
5	guanidinylated SBA-15/Fe <sub>3</sub> O <sub>4</sub>	0.02	EtOH	80	85
6	guanidinylated SBA-15/Fe <sub>3</sub> O <sub>4</sub>	0.02	H <sub>2</sub> O	100	<60
7	guanidinylated SBA-15/Fe <sub>3</sub> O <sub>4</sub>	0.02	EtOH/H <sub>2</sub> O (1:1)	80	95
8	guanidinylated SBA-15/Fe <sub>3</sub> O <sub>4</sub>	0.02	EtOH/H <sub>2</sub> O (1:1)	Ultrasonic, r.t	75
9	guanidinylated SBA-15/Fe <sub>3</sub> O <sub>4</sub>	0.01	EtOH/H <sub>2</sub> O (1:1)	80	76
10	guanidinylated SBA-15/Fe <sub>3</sub> O <sub>4</sub>	0.015	EtOH/H <sub>2</sub> O (1:1)	80	95
11	Fe <sub>3</sub> O <sub>4</sub>	0.015	EtOH/H <sub>2</sub> O (1:1)	80	N.R
12	SBA-15/Fe <sub>3</sub> O <sub>4</sub>	0.015	EtOH/H <sub>2</sub> O (1:1)	80	71
13	APTES@SBA-15/Fe <sub>3</sub> O <sub>4</sub>	0.015	EtOH/H <sub>2</sub> O (1:1)	80	84

**Table 2.** Optimizing the reaction conditions in the synthesis of dihydropyrano[2,3-c]pyrazole derivatives. <sup>a</sup>Reaction conditions: ethyl acetoacetate (1 mmol), hydrazine hydrate (1.2 mmol), 3-nitrobenzaldehyde (1 mmol) and malononitrile (1 mmol), catalyst (10–20 mg). <sup>b</sup>The yields relate to the isolated product.

SBA-15 pores and its subsequent functionalization, which resulted in less available surface area for gas adsorption. BJH pore size distributions of samples are depicted in Fig. 9(II), it is observed that the SBA-15/Fe<sub>3</sub>O<sub>4</sub> and guanidinylated SBA-15/Fe<sub>3</sub>O<sub>4</sub> samples has slightly more pore width (size) and also relatively broader pore size distributions compared to their precursor matrix.

**The catalytic application of guanidinylated SBA-15/Fe<sub>3</sub>O<sub>4</sub> nanocomposite.** The catalytic activity of the guanidinylated SBA-15/Fe<sub>3</sub>O<sub>4</sub> investigated in the synthesis of dihydropyrano [2, 3-c] pyrazole derivatives. To obtain the best result, different experimental conditions such as temperature, solvent, amount of catalyst and the type of catalysts was examined in the one-pot four components reaction of ethyl acetoacetate (1 mmol), hydrazine hydrate (1.2 mmol), 3-nitrobenzaldehyde (1 mmol) and malononitrile (1 mmol). First, the model reaction was performed without catalyst and solvent in two different temperatures, the yield of products was trace (Table 2, entries 1 and 2). By adding the guanidinylated SBA-15/Fe<sub>3</sub>O<sub>4</sub> catalyst to the model reaction in the absence of solvent, the yield of the reaction was reached about 47% (Table 2, entry 3). In the next step, to assess the solvent effect, ethanol was added to the reaction in the presence of a catalyst at room temperature, the efficiency increased considerably (Table 2, entry 4). Then, the reaction was repeated at 80° C to evaluate the effect of temperature and observed that increasing the temperature up to 80° C leads to the reaction progress (Table 2, entry 5). The subsequent optimization experiments were performed in H<sub>2</sub>O and EtOH/H<sub>2</sub>O as green media under reflux and ultrasonic conditions; the best efficiency was obtained in EtOH/H<sub>2</sub>O media at 80° C (Table 2, entries 6–8). In addition to reaction condition and solvent, various amounts of mesoporous nanocatalyst were tested and the maximum yield of product was achieved in the presence of 0.015 g catalyst (Table 2, entries 9 and 10). The efficiency of the prepared mesoporous nanocomposite compared with Fe<sub>3</sub>O<sub>4</sub>, SBA-15/Fe<sub>3</sub>O<sub>4</sub>, and APTES@SBA-15/Fe<sub>3</sub>O<sub>4</sub> in the model reaction was examined. As indicated in Table 2 (entries 11–13), the yield of a reaction in the presence of guanidinylated SBA-15/Fe<sub>3</sub>O<sub>4</sub> is higher than APTES@SBA-15/Fe<sub>3</sub>O<sub>4</sub>, SBA-15/Fe<sub>3</sub>O<sub>4</sub>, Fe<sub>3</sub>O<sub>4</sub>, respectively. Indeed, guanidinylated SBA-15/Fe<sub>3</sub>O<sub>4</sub> mesoporous nanocatalyst with dual active sites: base (primary and secondary amines), Lewis acid site (Fe<sup>3+</sup> in Fe<sub>3</sub>O<sub>4</sub>), high porosity and large surface area acted as an excellent catalyst to accelerate the synthesis of dihydropyrano [2,3-c] pyrazole derivatives via one-pot four-component reaction.

To assess the generality of the optimum conditions, a wide range of benzaldehydes bearing both electron-donating and electron-withdrawing substitution were tested. As is observed in Table 3, a wide range of substituted dihydropyrano[2,3-c]pyrazole derivatives were obtained in high yields by using guanidinylated SBA-15/Fe<sub>3</sub>O<sub>4</sub> mesoporous nanocatalyst in short reaction times.



Entry	R1	Product	Time (min)	Yield <sup>a</sup> (%)	Mp (°C)	
					Observed	Literature
1	2-Cl	5a	25	91	238–241	241–244 <sup>33</sup>
2	4-Cl	5b	20	92	230–232	232–233 <sup>24</sup>
3	2,4-Cl <sub>2</sub>	5c	30	90	196–198	198–199 <sup>25</sup>
4	2-NO <sub>2</sub>	5d	25	92	225–228	227–228 <sup>25</sup>
5	3-NO <sub>2</sub>	5e	20	95	196–198	195–196 <sup>34</sup>
6	4-Me	5f	20	93	202–204	204–206 <sup>33</sup>
7	3-OMe	5g	20	92	243–245	244–245 <sup>43</sup>
8	4-OMe	5h	30	92	208–210	210–212 <sup>24</sup>
9	3,4,5-(OMe) <sub>3</sub>	5i	40	89	208–211	210–212 <sup>24</sup>
10	3-OH	5j	30	89	255–257	253–256 <sup>35</sup>
11	4-OH	5k	25	90	223–225	223–225 <sup>24</sup>
12	3,4-(OH) <sub>2</sub>	5l	40	89	175–177	175–178 <sup>26</sup>
13	4-F	5m	20	96	203–205	205–207 <sup>26</sup>
14	4-CH(Me) <sub>2</sub>	5n	20	90	213–215	211–213 <sup>25</sup>
15	4-Br	5o	30	90	239–242	242–246 <sup>35</sup>
16	2-OH-5-Br	5p	30	95	226–228	226–227 <sup>24</sup>

**Table 3.** The synthesis of dihydropyrano[2,3-c] pyrazole derivatives in optimized condition using the guanidynylated SBA-15/Fe<sub>3</sub>O<sub>4</sub>. <sup>a</sup>The yields relate to the isolated product.

To assess the catalytic efficiency and advantages of the guanidynylated SBA-15/Fe<sub>3</sub>O<sub>4</sub> nanocomposite as an appropriate catalyst to promote the dihydropyrano[2,3-c], its catalytic activity in the synthesis of **5e** derivatives was compared with some other previously reported methods. As indicated in Table 4, the present method is superior to the other methods in terms of the yields of products or the reaction condition.

**Suggested mechanism.** As mention earlier, guanidynylated SBA-15/Fe<sub>3</sub>O<sub>4</sub> mesoporous nanocomposite with dual active sites: base (primary and secondary amines in guanidine groups), Lewis acid site (Fe<sup>3+</sup> in Fe<sub>3</sub>O<sub>4</sub>), high porous structure and large surface area, play an important role in all steps of this four-component reaction as illustrated in Fig. 10. As reported in the previous studies<sup>22,47</sup>, several main steps give the final product. First, the carbonyl groups of ethyl acetoacetate are activated by both amine group through hydrogen bonding and the Lewis acid site in the guanidynylated SBA-15/Fe<sub>3</sub>O<sub>4</sub> catalyst and then subjected to the nucleophilic attack of hydrazine hydrate with two nucleophilic sites. In this step, a pyrazolone ring is formed (intermediate I) by removing water and ethanol molecules, respectively. On the other hands, intermediate II (2-phenylidenemalononitrile) was produced through the Knoevenagel condensation reaction between catalysts-activated malononitrile (by strong basic sites of catalyst) and activated aromatic aldehyde (by hydrogen bond and Lewis acid site). Then, the Michael addition reaction between catalyst-activated the intermediate I and II, resulted in the compound III. The subsequent enolization and cyclization of intermediate III provided compound IV. Eventually, by tautomerization of molecule IV, dihydropyrano[2,3-c]pyrazole derivatives (**5a-p**) were obtained.

**Reusability evaluation of guanidynylated SBA-15/Fe<sub>3</sub>O<sub>4</sub> mesoporous catalyst.** The recovery and reusability of catalysts in catalytic reactions are important issues in term of the green chemistry<sup>21,28,55</sup>. The reusability of prepared mesoporous catalysts in the synthesis of pyranopyrazoles derivatives was evaluated in several runs. For this, after completion of the reaction, the catalyst was separated from the reaction mixture by a magnet, eluted by ethanol and dried in an oven at 60 °C for 6 h in order to be ready for the next catalytic run. Later, the recovered catalyst in a constant amount was used for the subsequent runs. The presented results in Fig. 11 revealed that the recycled catalyst could be effective at least six consecutive runs without considerable reduction in its catalytic activity.

Entry	Catalyst	Catalyst loading	Conditions	Yield <sup>a</sup> (%)	References
1	Lemon peel powder	10 wt%	EtOH, reflux	74	44
2	cetyltrimethylammonium chloride(CTACL)	20 mol%	H <sub>2</sub> O, 90 °C	90	45
3	OPC-SO <sub>3</sub> H	0.02g	EtOH, 80 °C	89	46
4	Molecular sieves (MS 4 Å)	10 ml	EtOH, reflux	84	47
5	Sodium ascorbate	15 mol%	H <sub>2</sub> O, reflux	84	48
6	BF <sub>3</sub> /MNPs	0.1 g	EtOH, 80 °C	91	49
7	TEA-Im-IL-Cu	200 ml	H <sub>2</sub> O, 80 °C	85	50
8	L-proline	10 mol%	H <sub>2</sub> O, reflux	87	51
9	nano-Al <sub>2</sub> O <sub>3</sub> /BF <sub>3</sub> /Fe <sub>3</sub> O <sub>4</sub>	0.03 g	EtOH / H <sub>2</sub> O, reflux	85	52
10	γ-alumina	30 mol%	H <sub>2</sub> O, reflux	75	53
11	Aspartic acid	20 mol%	EtOH / H <sub>2</sub> O, r.t	84	54
12	guanidinylated SBA-15/Fe <sub>3</sub> O <sub>4</sub>	0.03 g	EtOH / H <sub>2</sub> O, 80 °C	95	This work

**Table 4.** Comparison of the catalytic performance of the guanidinylated SBA-15/Fe<sub>3</sub>O<sub>4</sub> with some other reported catalysts for the synthesis of dihydropyrano[2,3-c]pyrazole (product 5e). <sup>a</sup>The yields relate to the isolated product.

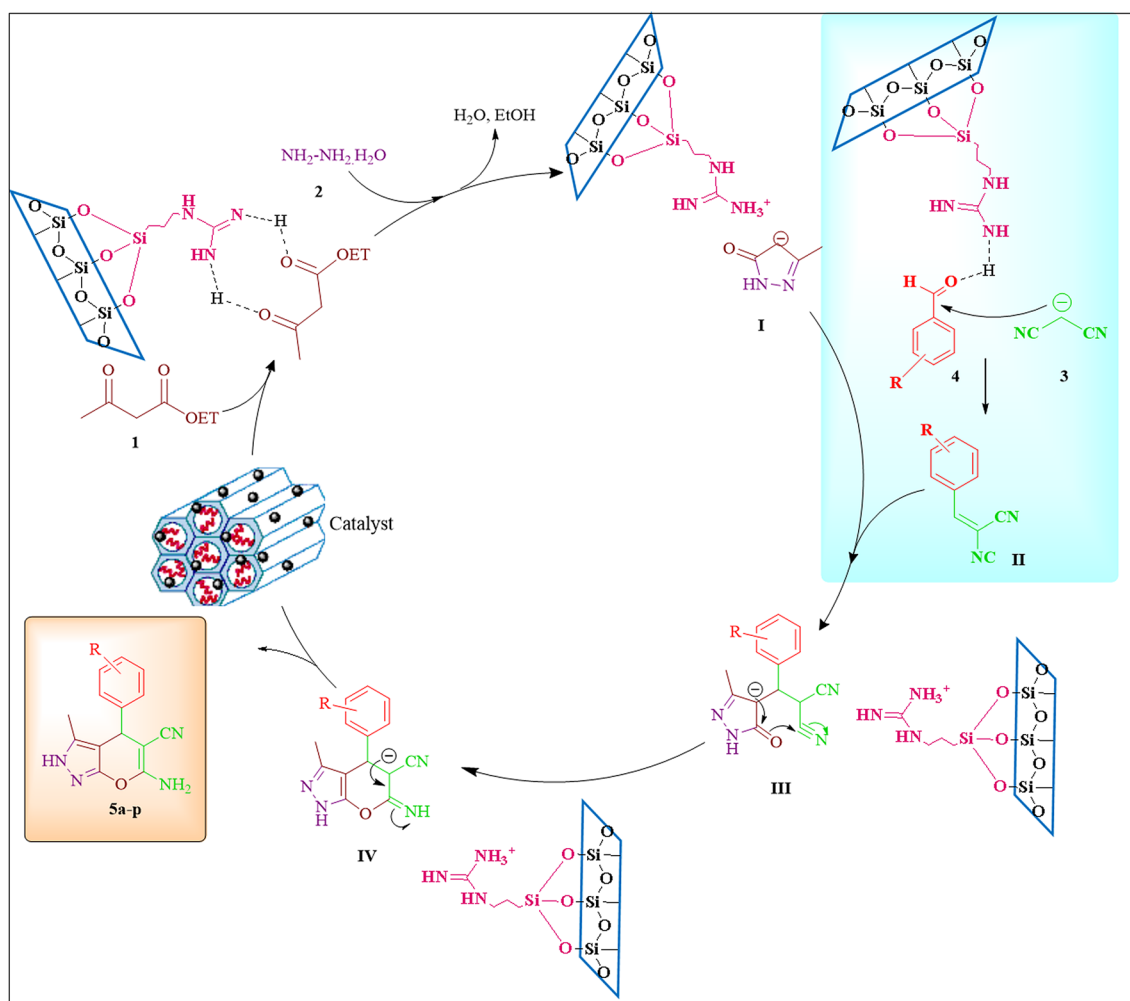


**Figure 10.** A suggested mechanism for the synthesis of pyrano[2,3-c]pyrazole derivatives catalyzed by the guanidinylated SBA-15/Fe<sub>3</sub>O<sub>4</sub>.

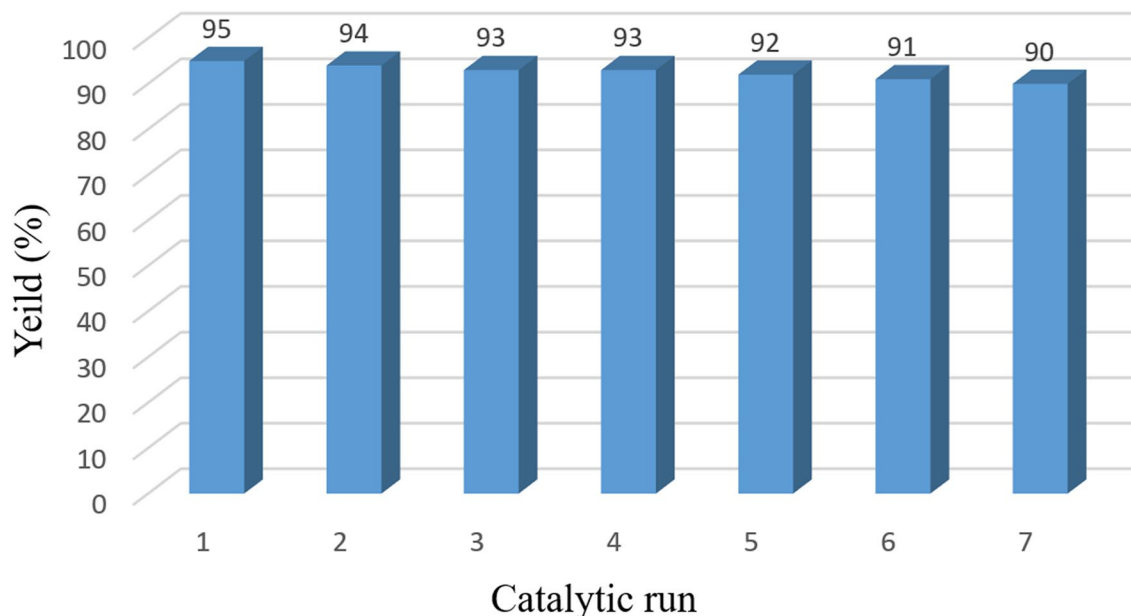


**Figure 11.** Recycling diagram of the guanidinylated SBA-15/Fe<sub>3</sub>O<sub>4</sub> mesoporous catalyst in the synthesis of **5e**.

## Conclusion

A novel mesoporous SBA-15 based nanocomposite prepared by modification of SBA-15 through *in-situ* construction of Fe<sub>3</sub>O<sub>4</sub> MNPs, consequent functionalization by APTES and finally guanidinylation reaction. This fabricated nanocomposite exhibited great catalytic performance in the synthesis of dihydropyrano pyrazole. The corresponding products were obtained in high yields without a complicated work-up procedure. The result of TGA analysis indicated that this nanocomposite has a very high thermal stability and has lost only about 15% of its weight up to 800 °C. The XRD pattern of nanocomposite in comparison with SBA-15 revealed that fabrication of Fe<sub>3</sub>O<sub>4</sub> MNPs with crystalline nature on SBA-15 porous support, even with two consecutive chemical modifications has enhanced its crystallinity. Moreover, presented peaks in diffractogram of guanidinylated SBA-15/Fe<sub>3</sub>O<sub>4</sub> mesoporous were in good agreement with characteristic peaks of SBA-15 and standard Fe<sub>3</sub>O<sub>4</sub>. The VSM analysis demonstrated the superparamagnetic property of nanocomposite with a Ms of about 12.2 emu/g. The FESEM images of SBA-15 and mesoporous nanocomposite showed the porous structure of SBA-15 and distribution of spherical shaped Fe<sub>3</sub>O<sub>4</sub> MNPs on SBA-15 support with an average size of about 26 nm. The FESEM of SBA-15 and mesoporous nanocomposite showed the porous structure of SBA-15 and distribution of spherical shaped Fe<sub>3</sub>O<sub>4</sub> MNPs on SBA-15 support with an average size of about 26 nm, and TEM images of nanocomposite exhibited both a regular mesoporous arrangement with two-dimensional hexagonal honeycomb structure and the Fe<sub>3</sub>O<sub>4</sub> MNPs onto SBA-15 support. Based on the suggested mechanism, the guanidinylated SBA-15/Fe<sub>3</sub>O<sub>4</sub> played a vital role in conducting the synthesis reaction of dihydropyrano[2,3-*c*] pyrazole derivatives with beneficial features such as strong basic sites, Lewis acid site, porous architecture and high surface area.

Received: 12 June 2021; Accepted: 21 September 2021

Published online: 06 October 2021

## References

1. Taguchi, A. & Schüth, F. Ordered mesoporous materials in catalysis. *Microporous Mesoporous Mater.* **77**(1), 1–45 (2005).
2. Chaudhary, V. & Sharma, S. An overview of ordered mesoporous material SBA-15: synthesis, functionalization and application in oxidation reactions. *J. Porous Mater.* **24**(3), 741–749 (2017).
3. Vernimmen, J., Meynen, V. & Cool, P. Synthesis and catalytic applications of combined zeolitic/mesoporous materials. *Beilstein J. Nanotechnol.* **2**(1), 785–801 (2011).
4. Wang, X., Lin, K. S. K., Chan, J. C. C. & Cheng, S. Direct synthesis and catalytic applications of ordered large pore aminopropyl-functionalized SBA-15 mesoporous materials. *J. Phys. Chem. B* **109**(5), 1763–1769 (2005).
5. Wang, S., Wang, K., Dai, C., Shi, H. & Li, J. Adsorption of Pb<sup>2+</sup> on amino-functionalized core-shell magnetic mesoporous SBA-15 silica composite. *Chem. Eng. J.* **262**, 897–903 (2015).
6. Vargas-Osorio, Z. *et al.* Novel synthetic routes of large-pore magnetic mesoporous nanocomposites (SBA-15/Fe<sub>3</sub>O<sub>4</sub>) as potential multifunctional theranostic nanodevices. *J. Mater. Chem. B* **5**(47), 9395–9404 (2017).
7. Hajiaghbabaei, L., Eslambolipour, M., Badieli, A., Ganjali, M. R. & Ziarani, G. M. Controlled release of anticancer drug using *o*-phenylenediamine functionalized SBA-15 as a novel nanocarrier. *Chem. Pap.* **75**(5), 1841–1850 (2021).
8. Ortiz-Bustos, J., Martín, A., Morales, V., Sanz, R. & García-Muñoz, R. A. Surface-functionalization of mesoporous SBA-15 silica materials for controlled release of methylprednisolone sodium hemisuccinate: Influence of functionality type and strategies of incorporation. *Microporous Mesoporous Mater.* **240**, 236–245 (2017).

9. González-Gómez, L., Gañán, J., Morante-Zarcelero, S., Pérez-Quintanilla, D. & Sierra, I. Sulfonic acid-functionalized SBA-15 as strong cation-exchange sorbent for solid-phase extraction of atropine and scopolamine in gluten-free grains and flours. *Foods* **9**(12), 1854 (2020).
10. Margolese, D., Melero, J. A., Christiansen, S. C., Chmelka, B. F. & Stucky, G. D. Direct syntheses of ordered SBA-15 mesoporous silica containing sulfonic acid groups. *Chem. Mater.* **12**(8), 2448–2459 (2000).
11. Wang, X., Lin, K. S. K., Chan, J. C. C. & Cheng, S. Preparation of ordered large pore SBA-15 silica functionalized with aminopropyl groups through one-pot synthesis. *Chem. Commun.* **23**, 2762–2763 (2004).
12. Kong, X., Gao, R., He, X., Chen, L. & Zhang, Y. Synthesis and characterization of the core-shell magnetic molecularly imprinted polymers ( $\text{Fe}_3\text{O}_4$ @MIPs) adsorbents for effective extraction and determination of sulfonamides in the poultry feed. *J. Chromatogr. A* **1245**, 8–16 (2012).
13. Hakiki, A. *et al.* Synthesis and characterization of mesoporous silica SBA-15 functionalized by mono-, di-, and tri-amine and its catalytic behavior towards Michael addition. *Mater. Chem. Phys.* **212**, 415–425 (2018).
14. Prasetyanto, E. A. & Park, S.-E. Synthesis of short-channelled amino-functionalized SBA-15 and its beneficial applications in base-catalyzed reactions. *Appl. Catal. A* **350**(2), 244–251 (2008).
15. Xu, L., Yao, F., Wang, C., Ye, M. & An, Y. Facile synthesis of amine-functionalized SBA-15-supported bimetallic Au-Pd nanoparticles as an efficient catalyst for hydrogen generation from formic acid. *RSC Adv.* **7**(8), 4746–4752 (2017).
16. Tameh, F. A., Safaei-Ghomi, J., Mahmoudi-Hashemi, M. & Shabazi-Alavi, H. One-pot multicomponent reaction synthesis of spirooxindoles promoted by guanidine-functionalized magnetic  $\text{Fe}_3\text{O}_4$  nanoparticles. *RSC Adv.* **6**(78), 74802–74811 (2016).
17. P. Selig, J. W. Shaw, D. H. Grayson, and I. Rozas, *Guanidines as Reagents and Catalysts I* 2017.
18. Zhai, X. *et al.* Guanidinylation: a simple way to fabricate cell penetrating peptide analogue-modified chitosan vector for enhanced gene delivery. *J. Appl. Polym. Sci.* **121**(6), 3569–3578 (2011).
19. Maleki, A., Firouzi-Haji, R. & Hajizadeh, Z. Magnetic guanidynated chitosan nanobiocomposite: a green catalyst for the synthesis of 1,4-dihydropyridines. *Int. J. Biol. Macromol.* **116**, 320–326 (2018).
20. Mattheis, C., Wang, H., Meister, C. & Agarwal, S. Effect of guanidinylation on the properties of Poly (2-aminoethylmethacrylate)-based antibacterial materials. *Macromol. Biosci.* **13**(2), 242–255 (2013).
21. Bahrami, S., Hassanzadeh-Afruzi, F. & Maleki, A. Synthesis and characterization of a novel and green rod-like magnetic ZnS/Cu $\text{Fe}_2\text{O}_4$ /agar organometallic hybrid catalyst for the synthesis of biologically-active 2-amino-tetrahydro-4H-chromene-3-carbonitrile derivatives. *Appl. Organomet. Chem.* **34**(11), 1–15 (2020).
22. Hajizadeh, Z., Hassanzadeh-Afruzi, F., Jelodar, D. E., Ahghari, M. R. & Maleki, A. Cu(ii) immobilized on  $\text{Fe}_3\text{O}_4$ @HNTs-tetrazole (CFHT) nanocomposite: synthesis, characterization, investigation of its catalytic role for the 1,3 dipolar cycloaddition reaction, and antibacterial activity. *RSC Adv.* **10**(44), 26467–26478 (2020).
23. Maleki, A., Hassanzadeh-Afruzi, F., Varzi, Z. & Esmaeili, M. S. Magnetic dextrin nanobiomaterial: an organic-inorganic hybrid catalyst for the synthesis of biologically active polyhydroquinoline derivatives by asymmetric Hantzsch reaction. *Mater. Sci. Eng. C* **109**, 110502 (2020).
24. Hajizadeh, Z. & Maleki, A. Poly(ethylene imine)-modified magnetic halloysite nanotubes: a novel, efficient and recyclable catalyst for the synthesis of dihydropyran[2,3-c]pyrazole derivatives. *Mol. Catal.* **460**(August), 87–93 (2018).
25. Maleki, A. & Eskandarpour, V. Design and development of a new functionalized cellulose-based magnetic nanocomposite: preparation, characterization, and catalytic application in the synthesis of diverse pyrano [2, 3-c] pyrazole derivatives. *J. Iran. Chem. Soc.* **16**(7), 1459–1472 (2019).
26. R. Eivazzadeh-Keihan *et al.*, *Fe<sub>3</sub>O<sub>4</sub>/GO@melamine-ZnO nanocomposite: a promising versatile tool for organic catalysis and electrical capacitance*, vol. 587 (Elsevier B.V., 2020).
27. Z. Amiri-Khamakani, F. Hassanzadeh-Afruzi, and A. Maleki, *Magnetized dextrin: Eco-friendly effective nanocatalyst for the synthesis of dihydropyran [2, 3-c] pyrazole derivatives* (2020).
28. Maleki, A., Varzi, Z. & Hassanzadeh-Afruzi, F. Preparation and characterization of an eco-friendly Zn $\text{Fe}_2\text{O}_4$ @alginate acid nanocomposite catalyst and its application in the synthesis of 2-amino-3-cyano-4H-pyran derivatives. *Polyhedron* **171**, 193–202 (2019).
29. H. Dogari, F. Hassanzadeh-Afruzi, and A. Maleki, *ZnFe<sub>2</sub>O<sub>4</sub> @ dimethylglyoxime : preparation and catalyst application in the synthesis of 2-amino- 1–5* (2020).
30. Hassanzadeh-Afruzi, F., Dogari, H., Esmailzadeh, F. & Maleki, A. Magnetized melamine-modified polyacrylonitrile (PAN@ melamine/ $\text{Fe}_3\text{O}_4$ ) organometallic nanomaterial: Preparation, characterization, and application as a multifunctional catalyst in the synthesis of bioactive dihydropyran [2, 3-c] pyrazole and 2-amino-3-cyano 4H-pyran derivatives. *Appl. Organomet. Chem.* **6**, e6363 (2021).
31. Dahaghin, Z., Zavvar, H. & Maryam, M. Synthesis and application of a novel magnetic SBA-15 nanosorbent for heavy metal removal from aqueous solutions. *J. Sol-Gel Sci. Technol.* **20**, 687 (2018).
32. de Ribeiro, J. O. N. *et al.* Role of the type of grafting solvent and its removal process on APTES functionalization onto SBA-15 silica for CO<sub>2</sub> adsorption. *J. Porous Mater.* **26**(6), 1581–1591 (2019).
33. Hair, M. L. Low-frequency infrared study. *Science* **2**, 923–927 (1991).
34. Juang, R.-S., Chien, C.-C., Yao, C.-L., Yu, S.-H. & Sun, A.-C. Preparation of magnetically recoverable mesoporous silica nanocomposites for effective adsorption of urea in simulated serum. *J. Taiwan Inst. Chem. Eng.* **91**, 22–31 (2018).
35. Ryu, S., Naidu, G., Moon, H. & Vigneshwaran, S. Selective copper extraction by multi-modified mesoporous silica material, SBA-15. *Sci. Total Environ.* **697**, 134070 (2019).
36. Szegedi, A., Popova, M., Goshev, I. & Mihály, J. Effect of amine functionalization of spherical MCM-41 and SBA-15 on controlled drug release. *J. Solid State Chem.* **184**(5), 1201–1207 (2011).
37. Maleki, A., Firouzi-Haji, R. & Hajizadeh, Z. Magnetic guanidynated chitosan nanobiocomposite: a green catalyst for the synthesis of 1,4-dihydropyridines. *Int. J. Biol. Macromol.* **116**, 320–326 (2018).
38. Cheng, Q. *et al.* Conducting polypyrrole confined in ordered mesoporous silica SBA-15 channels: preparation and its electrorheology. *Microporous mesoporous Mater.* **93**(1–3), 263–269 (2006).
39. Luan, Z., Fournier, J. A., Wooten, J. B. & Miser, D. E. Preparation and characterization of (3-aminopropyl) triethoxysilane-modified mesoporous SBA-15 silica molecular sieves. *Microporous mesoporous Mater.* **83**(1–3), 150–158 (2005).
40. Wu, Q. *et al.* Development and application of immobilized surfactant in mass spectrometry-based proteomics. *RSC Adv.* **7**(70), 44282–44288 (2017).
41. Vojoudi, H. *et al.* Post-modification of nanoporous silica type SBA-15 by bis (3-triethoxysilylpropyl) tetrasulfide as an efficient adsorbent for arsenic removal. *Powder Technol.* **319**, 271–278 (2017).
42. Adibmehr, Z. & Faghihian, H. Preparation of highly selective magnetic cobalt ion-imprinted polymer based on functionalized SBA-15 for removal Co<sup>2+</sup> from aqueous solutions. *J. Environ. Heal. Sci. Eng.* **17**(2), 1213–1225. <https://doi.org/10.1007/s40201-019-00439-x> (2020).
43. Kashtoh, H. *et al.* Dihydropyran [2, 3-c] pyrazole: novel in vitro inhibitors of yeast  $\alpha$ -glucosidase. *Bioorg. Chem.* **65**, 61–72 (2016).
44. Ghodke, S. S. *et al.* One-pot synthesis of pyrano [2, 3-c] pyrazoles using lemon peel powder as a green and natural catalyst. *Eur. Chem. Bull.* **9**(2), 38–42 (2020).
45. Wu, M., Feng, Q., Wan, D. & Ma, J. CTACl as catalyst for four-component, one-pot synthesis of pyranopyrazole derivatives in aqueous medium. *Synth. Commun.* **43**(12), 1721–1726 (2013).

46. Nagasundaram, N., Kokila, M., Sivaguru, P., Santhosh, R. & Lalitha, A. SO<sub>3</sub>H@ carbon powder derived from waste orange peel: an efficient, nano-sized greener catalyst for the synthesis of dihydropyran [2, 3-c] pyrazole derivatives. *Adv. Powder Technol.* **31**(4), 1516–1528 (2020).
47. Gujar, J. B., Chaudhari, M. A., Kawade, D. S. & Shingare, M. S. Molecular sieves: an efficient and reusable catalyst for multi-component synthesis of dihydropyran [2, 3-c] pyrazole derivatives. *Tetrahedron Lett.* **55**(44), 6030–6033 (2014).
48. Kiyani, H. & Bamdad, M. Sodium ascorbate as an expedient catalyst for green synthesis of polysubstituted 5-aminopyrazole-4-carbonitriles and 6-amino-1, 4-dihydropyran [2, 3-c] pyrazole-5-carbonitriles. *Res. Chem. Intermed.* **44**(4), 2761–2778 (2018).
49. Abdollahi-Alibeik, M., Moaddeli, A. & Masoomi, K. BF<sub>3</sub> bonded nano Fe<sub>3</sub>O<sub>4</sub> (BF<sub>3</sub>/MNPs): an efficient magnetically recyclable catalyst for the synthesis of 1, 4-dihydropyran [2, 3-c] pyrazole derivatives. *RSC Adv.* **5**(91), 74932–74939 (2015).
50. Ghafari, H., Leili, M. K. & Zand, H. R. E. Copper-immobilized ionic liquid as an alternative to organic solvents in the one-pot synthesis of bioactive dihydropyran [2, 3-c] pyrazole derivatives. *Appl. Organomet. Chem.* **34**(9), e5757 (2020).
51. Mecadon, H. *et al.* L-Proline as an efficient catalyst for the multi-component synthesis of 6-amino-4-alkyl/aryl-3-methyl-2, 4-dihydropyran [2, 3-c] pyrazole-5-carbonitriles in water. *Tetrahedron Lett.* **52**(25), 3228–3231 (2011).
52. Babaei, E. & Mirjalili, B. B. F. An expedient and eco-friendly approach for multicomponent synthesis of dihydropyran [2, 3-c] pyrazoles using nano-Al<sub>2</sub>O<sub>3</sub>/BF<sub>3</sub>/Fe<sub>3</sub>O<sub>4</sub> as reusable catalyst. *Inorg. Nano-Metal Chem.* **50**(1), 16–21 (2020).
53. Mecadon, H., Rohman, M. R., Rajbangshi, M. & Myrboh, B. γ-Alumina as a recyclable catalyst for the four-component synthesis of 6-amino-4-alkyl/aryl-3-methyl-2, 4-dihydropyran [2, 3-c] pyrazole-5-carbonitriles in aqueous medium. *Tetrahedron Lett.* **52**(19), 2523–2525 (2011).
54. Ahad, A. & Farooqui, M. Organocatalyzed domino reactions: diversity oriented synthesis of pyran-annulated scaffolds using in situ-developed benzylidenemalononitriles. *Res. Chem. Intermed.* **43**(4), 2445–2455 (2017).
55. Eivazzadeh-keihan, R., Bahreinizad, H., Amiri, Z. & Madanchi, H. Trends in Analytical Chemistry Functionalized magnetic nanoparticles for the separation and purification of proteins and peptides. *Science* **141**, 15000 (2021).

## Acknowledgements

All authors gratefully acknowledge the partial support from the Research Council of the Iran University of Science and Technology. This work is upon research funded by Iran National Science Foundation (INSF) under project No. 99032872.

## Author contributions

F.H.-A. Conceptualization-Supporting, Data curation, Formal analysis-Equal, Investigation-Equal, Methodology-Equal, Validation, Writing-original draft-Equal, Somayeh Asgharnasl Formal analysis-Equal, Methodology-Equal, Writing-original draft-Equal, S.M. Formal analysis, Methodology-Equal, Z.A.-K. Investigation-Equal, Methodology-Equal, A.M. Conceptualization-Lead, Funding acquisition-Lead, Project administration-Equal, Supervision-Lead.

## Competing interests

The authors declare no competing interests.

## Additional information

**Supplementary Information** The online version contains supplementary material available at <https://doi.org/10.1038/s41598-021-99120-3>.

**Correspondence** and requests for materials should be addressed to A.M.

**Reprints and permissions information** is available at [www.nature.com/reprints](http://www.nature.com/reprints).

**Publisher's note** Springer Nature remains neutral with regard to jurisdictional claims in published maps and institutional affiliations.



**Open Access** This article is licensed under a Creative Commons Attribution 4.0 International License, which permits use, sharing, adaptation, distribution and reproduction in any medium or format, as long as you give appropriate credit to the original author(s) and the source, provide a link to the Creative Commons licence, and indicate if changes were made. The images or other third party material in this article are included in the article's Creative Commons licence, unless indicated otherwise in a credit line to the material. If material is not included in the article's Creative Commons licence and your intended use is not permitted by statutory regulation or exceeds the permitted use, you will need to obtain permission directly from the copyright holder. To view a copy of this licence, visit <http://creativecommons.org/licenses/by/4.0/>.

© The Author(s) 2021